Materials Characterization 178 (2021) 111284

Contents lists available at ScienceDirect

Materials Characterization

journal homepage: www.elsevier.com/locate/matchar

On prominent TRIP effect and non-basal slip in a TWIP high entropy alloy during high-pressure torsion processing

A.K. Chandan [a,b,*], P.T. Hung [c], K. Kishore [a,d], M. Kawasaki [e], J. Chakraborty [a,b], J. Gubicza [c,**]

[a] Academy of Scientific and Innovative Research (AcSIR), Ghaziabad 201002, India
[b] Materials Engineering Division, National Metallurgical Laboratory CSIR, Jamshedpur 831007, India
[c] Department of Materials Physics, Eötvös Loránd University, P.O.B. 32, Budapest H-1518, Hungary
[d] Research & Development and Scientific Services, Tata Steel Limited, Jamshedpur 831007, India
[e] School of Mechanical, Industrial and Manufacturing Engineering, Oregon State University, Corvallis, OR 97331, USA

ARTICLE INFO

Keywords:
Transformative HEA
TWIP HEA
High pressure torsion
c/a ratio
Non-basal slip

ABSTRACT

Severe plastic deformation response of a face centered cubic (FCC) twinning induced plasticity (TWIP) high entropy alloy (HEA), $Fe_{40}Mn_{40}Co_{10}Cr_{10}$, subjected to high-pressure torsion (HPT) is investigated. The so-called TWIP HEA demonstrated an extensive transformation induced plasticity (TRIP) effect even in ½ turn (shear strain, $\gamma = 15$) of HPT processing, which increased further with increasing the number of turns to 2 ($\gamma = 68$). Additionally, HPT induced nano-structuring and heavily dislocated structure; dislocation density was of the order of 10^{15} m^{-2}. c/a ratio of the transformed HCP phase was found to be <1.633 and it did not change with increasing the extent of shear strain. This was manifested as the occurrence of at least 50% non-basal slip in the HCP phase. For the first time, the fraction of <c> and <c+a> dislocations are quantified and their evolution are discussed in the purview of the studied alloy. The micro-mechanism of strain accommodation is correlated with increasing hardness of the HEA upon sequential HPT processing. The present work provides a viewpoint that the deformation induced HCP phase in a metastable FCC HEA can have tailored c/a ratio which triggers non-basal slip, leading to a strong and ductile material.

1. Introduction

Last few years have witnessed the emergence of several face centred cubic (FCC) transformative high entropy alloy (HEA) owing to their prowess to achieve superior strength-ductility combination [1–5]. FCC (γ) phase in such transformative HEA is metastable which transforms to hexagonal close-packed (HCP) phase (ε) during deformation [2,3,5], thus contributes to the work hardening via the Transformation-Induced Plasticity (TRIP) mechanism. Further, the prior presence of HCP phase can aid to work hardening at the later stage of deformation by formation of stacking faults and twins [3]. Hence, dual work hardening can be obtained in FCC HEAs, first, by the inherently present HCP phase and second, by the TRIP mechanism in the metastable FCC phase. HCP phase has been shown to be the stable phase in various FCC HEAs [6–9]. However, recent studies have revealed very high energy barrier for the $\gamma \rightarrow \varepsilon$ transformation [10,11]. This necessitates application of high stresses to form ε phase, which cannot be achieved by conventional processing techniques. For instance, $\gamma \rightarrow \varepsilon$ transformation in the equiatomic FeMnCoCrNi alloy is possible only at application of extremely high pressure of the order of ~14 GPa [11]. This indicates towards the kinetically constrained nature of the $\gamma \rightarrow \varepsilon$ transformation at ambient condition. In this context, grain refinement of the γ phase can possibly trigger the $\gamma \rightarrow \varepsilon$ phase transformation, since the probability of formation of planar faults increases with decreasing grain size [12,13], and intrinsic faulting in every second (111) plane in FCC phase yields the development of a HCP phase [14]. Severe plastic deformation (SPD) technique such as high-pressure torsion (HPT) can be utilized for grain refinement and thereby trigger the required phase transformation.

Presence of HCP phase in the microstructure, however, is considered to be deleterious in terms of mechanical properties (ductility/toughness) due to limited availability of dislocation slip systems, leading to non-compliance with respect to the Taylor – von Mises criterion of accommodation of arbitrary plastic deformation in a polycrystalline material [15]. Such a condition can render the alloy brittle and therefore, it is

* Correspondence to: A. K. Chandan, MTE Division, CSIR-NML, P.O.: Burmamines, Jamshedpur 831007, Jharkhand, India.
** Correspondence to: J. Gubicza, Department of Materials Physics, Eötvös Loránd University, P.O.B. 32, Budapest H-1518, Hungary.
E-mail addresses: avanish@nmlindia.org (A.K. Chandan), jeno.gubicza@ttk.elte.hu (J. Gubicza).

https://doi.org/10.1016/j.matchar.2021.111284
Received 12 February 2021; Received in revised form 3 June 2021; Accepted 23 June 2021
Available online 26 June 2021

required to activate non-basal slip along with the conventional basal slip. Activation of the so-called 'hard orientation', i.e., non-basal slip is highly dependent on the c/a ratio of the HCP phase [16]. c/a ratio can be altered by adjusting the alloy composition suitably [17]. The concept of HEA provides enormous possibility of composition modification, thereby tuning the c/a ratio. In addition to this, Sinha et al. have recently presented the possibility of deformation assisted alteration of the c/a ratio in HEAs [4]. The particular paper, however, did not show the formation of various non-basal dislocations and the associated quantification was missing [4]. Furthermore, there is no study which deals about the evolution of type and density of dislocations in a transformative HEA during HPT processing.

In the present work, we investigate the dislocation plasticity of the newly formed HCP phase in a HPT-processed $Fe_{40}Mn_{40}Co_{10}Cr_{10}$ (atomic %) HEA which otherwise is classically believed to be a Twinning-Induced Plasticity (TWIP) HEA [18]. We showcase the occurrence of non-basal slip in the HCP phase by demonstrating a deformation-induced c/a ratio lesser than the ideal value of 1.633. The quantified information of <c> and <c+a> dislocation formation is reported for the first time in the $Fe_{40}Mn_{40}Co_{10}Cr_{10}$ HEA, employing the X-ray diffraction line profile analysis (XLPA), and microstructural study by transmission electron microscopy (TEM) and electron backscattered diffraction (EBSD). Interestingly, this alloy demonstrated an absence of conventional grain refinement during HPT processing which seems to be counter-intuitive [19]. Hence, the possibility of microstructural refinement to nano-scale during HPT processing was also investigated.

2. Materials and methods

2.1. Processing of the material

HEA with the composition of $Fe_{40}Mn_{40}Co_{10}Cr_{10}$ (at.%) was fabricated by vacuum arc melting of 99.9% pure constituent elements. The cast ingot was homogenized at 1200 °C for 1.5 h and subsequently forged to a plate of thickness 10 mm. The forged plate was further hot rolled at a finish rolling temperature of 1000 °C in order to reduce the thickness to 6 mm. The hot rolled plate was subsequently reduced to a final thickness of 2 mm via cold rolling. The cold rolled material was subjected to solution annealing treatment at 900 °C for 25 min, followed by water quenching. Circular discs with a thickness of ~0.9 mm and a diameter of ~10 mm were manufactured for HPT processing. The disc specimens were subjected to a conventional HPT processing with quasi-constrained set-up [20]. Schematic of the HPT processing and processing parameters is shown in Fig. 1(a). HPT processing was performed for 1/2 and 2 turns, at room temperature with an applied pressure of 6 GPa at 1 rpm. The shear strain (γ) along the radius direction produced during HPT deformation varies with number of rotation (n), distance of point of interest from centre of disk (r) and thickness of the specimen as [21]:

$$\gamma = \frac{2\pi rn}{< t >} \quad (1)$$

where, $< t > = (t_i + t_f)/2$; t_i and t_f are initial and final thickness, respectively. Based on the Eq. (1), the shear strain values for the ½ turn and 2 turns processed specimens are ~15 and ~ 68, respectively. For comparison of microstructure evolution, a generalized entity, i.e., the shear strain has been considered which takes into account all the HPT variables.

2.2. Microstructural characterization

The HPT processed specimens were studied using X-ray diffraction (XRD), EBSD and TEM. Microstructural investigations were performed 4 mm away from the centers of the discs, i.e., near the edge of the sample. Fig. 1(b) depicts the schematic of HPT processed specimen showing the location of microstructural investigation. Specimens for the EBSD and XRD investigations were prepared by firstly mechanical polishing using SiC abrasive paper, followed by electropolishing the specimen in an ethanol + perchoric acid solution (90:10), maintained at −25 °C, at 18 V. ESBD was performed in HITACHI SU700 FESEM equipped with EDAX Velocity EBSD detector. The step size for the EBSD characterization was kept to be 40 nm. For TEM characterization, specimens were first mechanically thinned down to a level of 60 μm, followed by twin jet polishing in an ethanol + perchoric acid solution (90:10) maintained at −25 °C, in order to make the specimen electron transparent. TEM investigation was performed in a JEOL JEM 2200FS equipment, which was operated at 200 kV.

2.3. X-ray line profile analysis

XLPA was performed to discern the evolution of various microstructural parameters during the HPT processing. XRD patterns were measured by a Smartlab diffractometer (manufacturer: Rigaku, Japan) using θ-θ measurement mode with parallel beam and CuKα$_1$ radiation. The beam length was 2 mm perpendicular to the plane of the incident and the detected scattered beams. The beam width was 0.25 mm which yielded an illuminated surface width of ~0.33–0.73 mm depending on the diffraction angle. The typical 2θ angle range was 35-105^o for all the measurements.

The XRD patterns were evaluated for the crystallite (or diffraction domain) size and the dislocation density using the methodology of XLPA

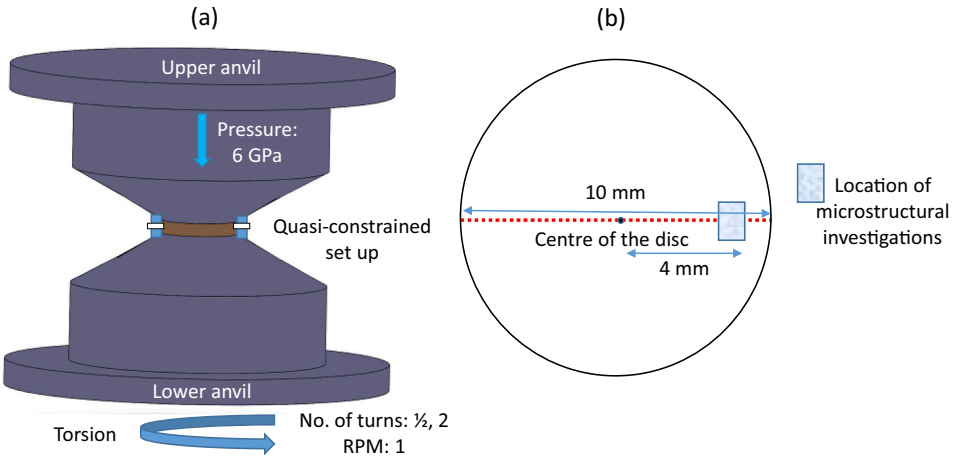

Fig. 1. (a) Schematic of the HPT processing showing the details of the processing parameters; (b) schematic of the HPT processed disc and the location of the microstructural investigation.

[22]. The evaluation was carried out by the convolutional multiple whole profile (CMWP) fitting procedure [23]. In this method, the diffraction pattern is fitted by the sum of a background spline and theoretical peak profiles. The latter ones are obtained as the convolution of the instrumental peak and the calculated line profiles related to the crystallite size and dislocations. In the present case, instrumental correction was not applied due to the high breadth of the measured peaks. The CMWP fitting yielded the area-weighted mean crystallite size ($<x>_{area}$) and the dislocation density (ρ) where the former quantity was obtained from the median (m) and the lognormal variance of the crystallite size distribution (σ^2) as $<x>_{area} = m \cdot \exp.(2.5\sigma^2)$.

The distribution of dislocations among the active dislocation slip systems was determined from parameters q_1 and q_2 which were also obtained from the CMWP method. In this procedure, the experimentally determined values of q_1 and q_2 are compared with the theoretical values calculated for the eleven possible dislocation types in the main hcp phase of $Fe_{40}Mn_{40}Co_{10}Cr_{10}$ [24]. The theoretical q_1 and q_2 parameters for the different dislocation types can be determined from the anisotropic elastic constants of the material using the software ANIZC (http://metal.elte.hu/anizc) [25]. Since, for the present hcp $Fe_{40}Mn_{40}Co_{10}Cr_{10}$ alloy the single crystal elastic constants were not available in the literature, the values obtained for a similar composition of $Fe_{50}Mn_{30}Co_{10}Cr_{10}$ [26] were applied in the program ANIZC, yielding the theoretical q_1 and q_2 parameters for the eleven dislocation types. Then, these theoretical q_1 and q_2 values were used in the software Hexburger which determined the population of the different dislocation types by comparing the experimentally measured q_1 and q_2 with the theoretical values averaged for different fractions of the eleven dislocation types. A more detailed description of this method can be found in [22].

2.4. Hardness measurement

Hardness measurement was performed using Vickers hardness tester (EMCO) at a load of 500 g and dwell time of 30 s. Hardness measurement was done 4 mm away from the centers of the discs, i.e., near the edge of the sample. At least five indentations were performed to evaluate the average hardness.

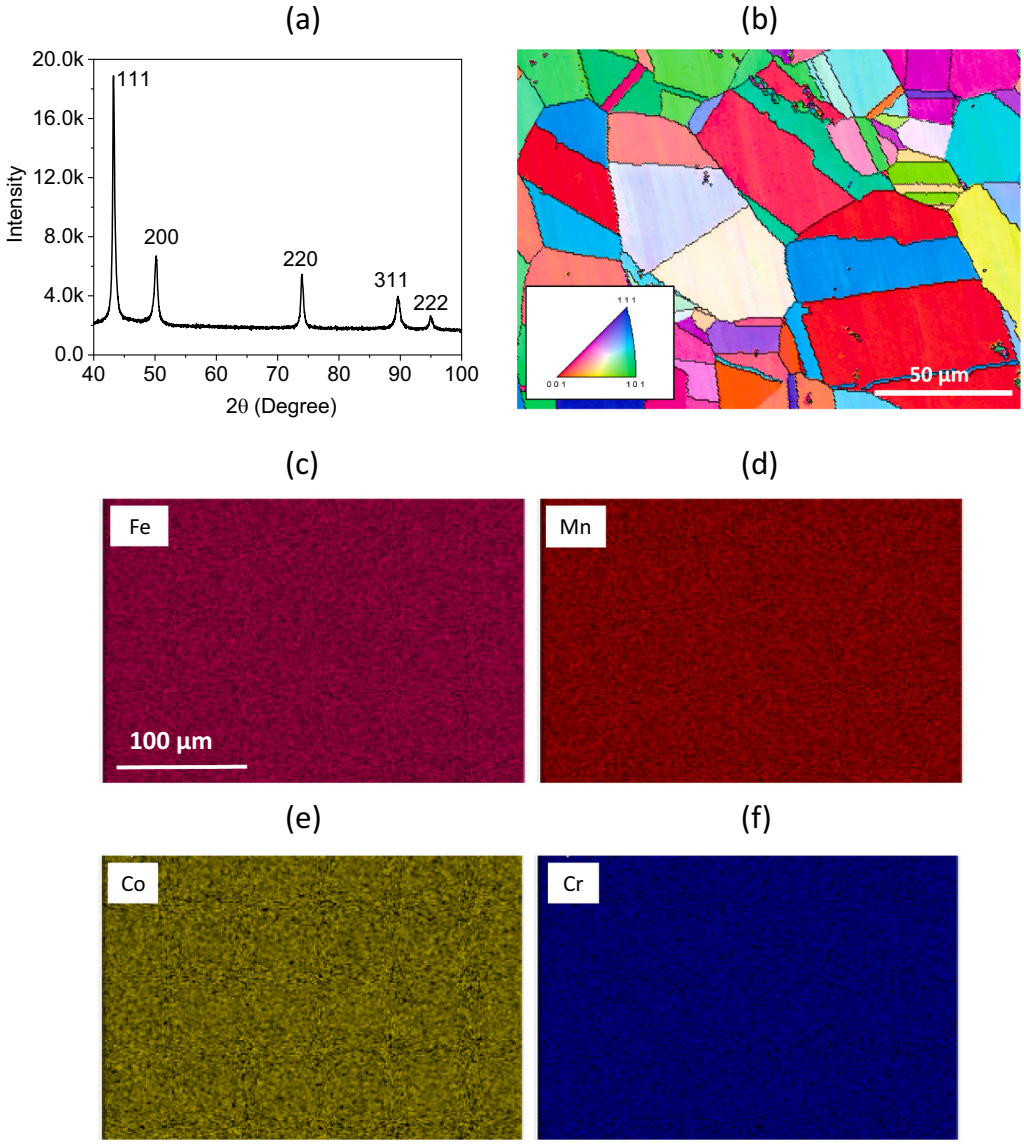

Fig. 2. (a) Indexed XRD pattern; (b) EBSD IPF map of the starting material; SEM-EDS map of (c) iron; (d) manganese; (e) cobalt; (f) chromium in the starting material.

3. Results

3.1. Initial and HPT-processed microstructures

Fig. 2(a) presents the XRD pattern of the starting material that is in the cold rolled and solution annealed condition. The XRD pattern is indexed with respect to a FCC structure which infers that the microstructure of the starting material was a single phase FCC microstructure. Fig. 2(b) displays the EBSD inverse pole figure (IPF) map of the starting material. The average grain size of the initial material, excluding annealing twins, was 36 ± 7 μm. The starting material was chemically homogenous, i.e., free from any elemental segregation. Fig. 2(c–f) presents the energy dispersive spectroscopy (EDS) maps of various constituent elements in the alloy, showing homogenous distribution of elements.

Fig. 3(a) presents the XRD patterns of the HPT-processed specimens. The HPT-processed specimens underwent a $\gamma \rightarrow \varepsilon$ transformation and therefore the patterns were indexed with respect to the FCC and HCP phases. Apparently, the deformation-induced $\gamma \rightarrow \varepsilon$ phase transformation occurred enormously during HPT processing even up to $\gamma = 15$, rendering the matrix depleted of FCC phase and the HCP became the major phase. Estimations of the volume fractions of phases were performed by employing the Material Analysis Using Diffraction (MAUD) software package [27]. Quality of curve fitting using the MAUD program is shown in Fig. 3(b) for the HPT-processed specimens. A table in the inset of the Fig. 3(b) presents the volume % of HCP phase and the calculated c/a ratio in HPT-processed specimens. Volume % of the deformation induced HCP phase was ~75 and ~ 91 at $\gamma = 15$ and 68, respectively. Sathiyamoorthi et al. reported the $\gamma \rightarrow \varepsilon$ phase transformation in the presently studied alloy during HPT processing at a relatively lower nominal pressure of 4 GPa in comparison to 6 GPa in the present study [19]. They showed up to 60 vol% of HCP phase formed during the HPT processing of 1 turn [19]. Hence, the occurrence of 91 vol% of HCP phase after 2 turns HPT processing at 6 GPa nominal pressure in the present case is in line with the literature. c/a ratio of the HCP phase was calculated from the lattice parameters obtained after the MAUD fitting. c/a ratio remained nearly constant at ~1.62 during HPT through 2 turns.

Fig. 4(a) presents the STEM bright field micrograph of the specimen HPT-processed at $\gamma = 68$. The micrograph possessed various contrast which corresponds to the formation of defects and HCP phase. Fig. 4 (b–e) show the STEM-EDS maps of the constituent elements present in the alloy. No compositional inhomogeneity was observed after the HPT processing up to $\gamma = 68$, as is evident from the uniform elemental maps in Fig. 4(b–e). STEM-EDS mapping was performed for a small region with a spot size of 0.7 nm in order to clearly capture the compositional differences, if at all associated with the $\gamma \rightarrow \varepsilon$ phase transformation.

Fig. 5(a) and (c) present the EBSD IPF maps corresponding to shear strains of $\gamma = 15$ and 68, respectively. Corresponding phase maps are presented in Fig. 5(b) and (d), respectively. Evidently, the fraction of unindexed points increased on increasing γ from 15 to 68, indicating a greater distortion in the lattice in the latter case, which is perhaps caused by to a high dislocation generation for accommodation of large strain during the HPT processing. It is apparent from the IPFs that the grain refinement is more prominent in the specimen which suffered greater shear strain (i.e., $\gamma = 68$). Furthermore, the fraction of transformed HCP phase increased from ~69% to ~90% with increase in shear strain from 15 to 68. This observation is in line with the phase fraction determined using the XRD technique (Fig. 3(b)). Minor difference in the phase fractions obtained using EBSD and XRD techniques could be due to difference in the scanned volume in the two cases. EBSD considered very small area, which resulted in the disparity in the estimated phase fraction in the two cases for the same specimen. In this regard, data obtained from XRD should be considered representative owing to much larger scanned volume than that from EBSD.

TEM investigation at $\gamma = 15$ also indicated an extensive formation of HCP phase. Fig. 6(a) presents a bright-field (BF) TEM micrograph showing the formation of HCP lamellae. Corresponding selected area diffraction pattern (SADP) revealed the HCP lamellae of two different variants of the $< 11\bar{2}0 >$ zone axis, in coexistence with the FCC matrix with the $\langle 011 \rangle$ zone axis (Fig. 6(b)). Thus, FCC and HCP phases obey the Shoji–Nishiyama (S—N) orientation relationship, which is given as:

$$(111)_\gamma // (0001)_\varepsilon$$

$$\left[10\bar{1}\right]_\gamma // \left[11\bar{2}0\right]_\varepsilon$$

Fig. 6(c) and (d) present the dark-field (DF) TEM micrographs showing the two distinct variants of the HCP phase. Dark field micrographs were obtained from the encircled diffraction spots in Fig. 6(b). TEM investigation of the HEA at $\gamma = 68$ revealed the highly dislocated structure corresponding to the $\left\{0\bar{1}11\right\}$ family planes. Fig. 7(b) presents a TEM DF micrograph taken using the $0\bar{1}11$ diffraction spot of the HCP phase, highlighting the $(0\bar{1}11)$ plane which sustained rigorous dislocation-induced deformation. Accordingly, the phase boundaries were demarcated in the BF TEM micrograph (Fig. 7(a)). The $\left(0\bar{1}11\right)$ plane is one of the pyramidal planes, hence, dislocations causing slip in a consistent way can be either <a> type and/or <c+a> type, suggesting non-basal slips might occur in the HCP phase.

Further, the investigation of the HPT processed specimens revealed formation of HCP nano-crystallites. Fig. 8(a) displays the TEM BF micrograph of the specimen processed up to $\gamma = 15$, showing HCP lamellae. It is important to note that the size of the newly formed HCP

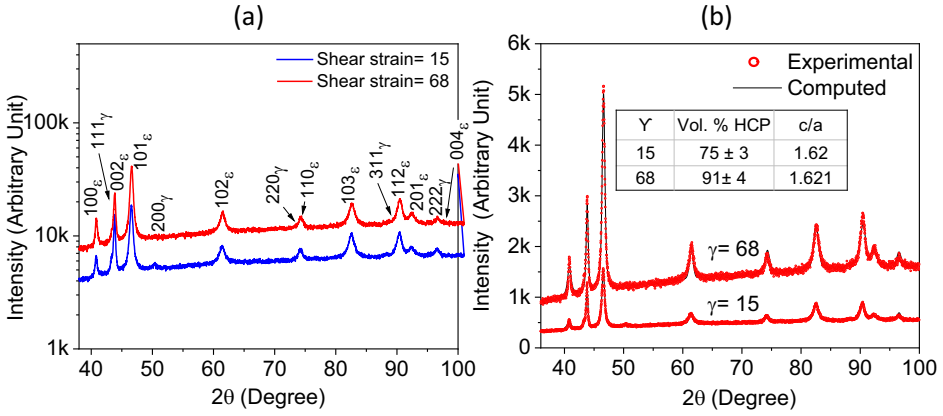

Fig. 3. (a) Indexed XRD pattern of HPT-processed specimens at $\gamma = 15$ and 68 showing formation of significant amount of HCP phase; (b) MAUD fitting of the experimentally obtained XRD patterns for volume fraction calculation.

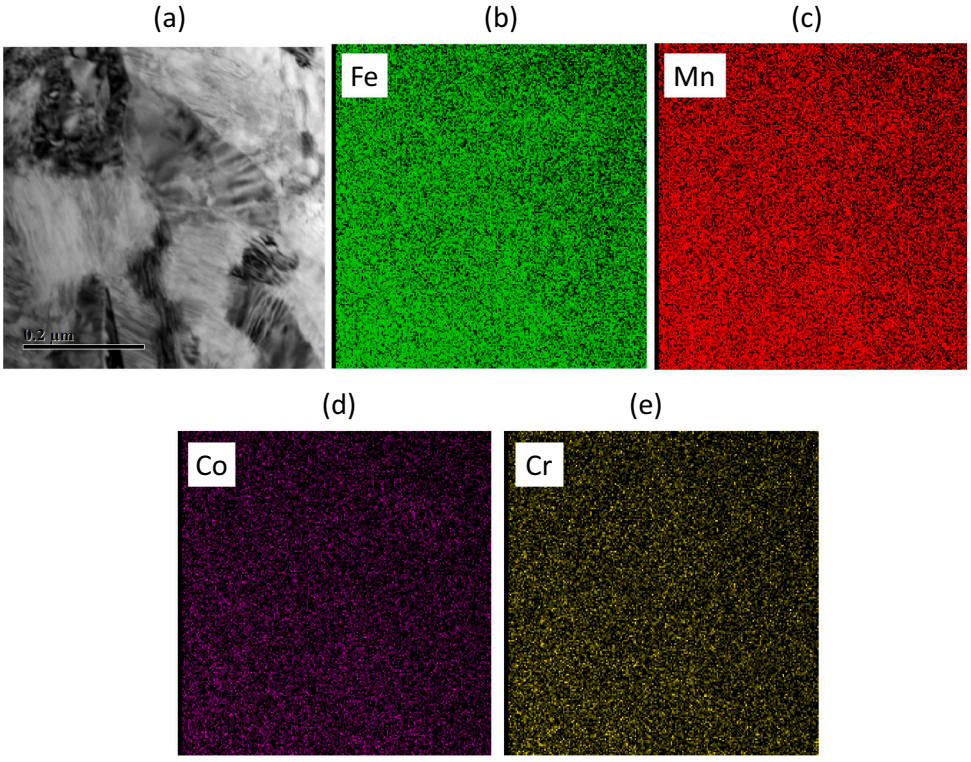

Fig. 4. (a) STEM bright field micrograph of the specimen HPT-processed up to $\gamma = 68$; STEM-EDS map of (c) iron; (d) manganese; (e) cobalt; (f) chromium in the HPT-processed material.

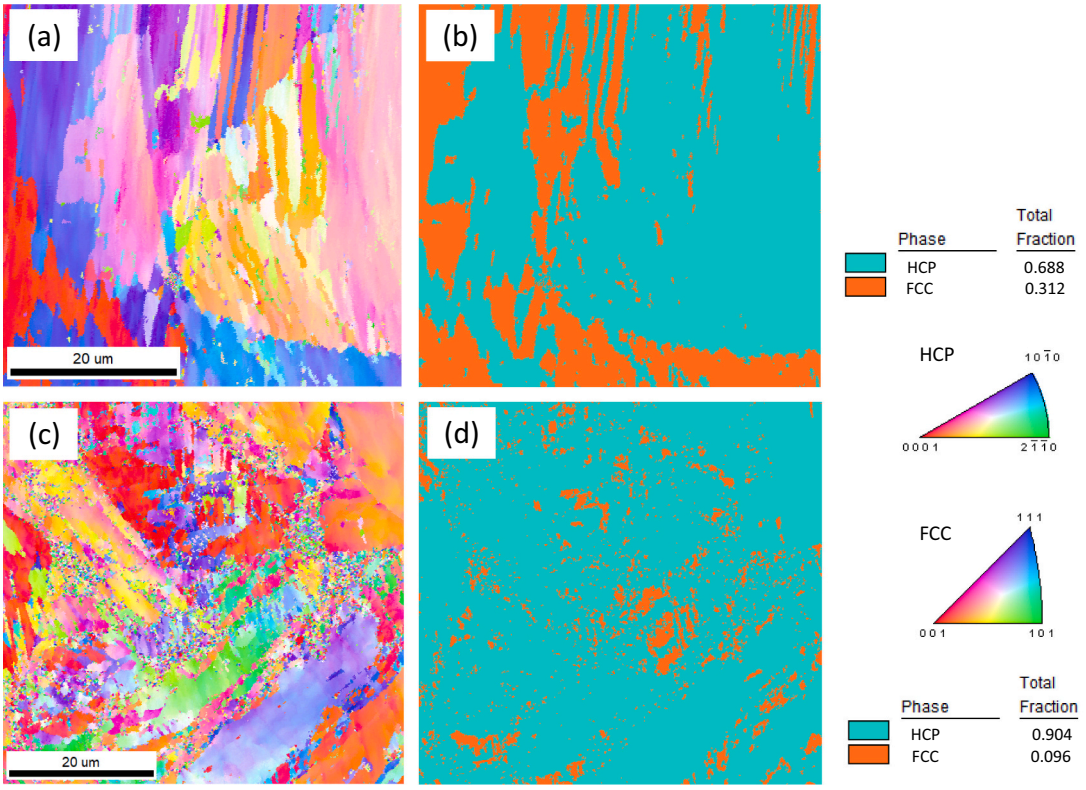

Fig. 5. (a) EBSD IPF map and (b) phase map for the specimen processed up to $\gamma = 15$. (c) EBSD IPF map and (d) phase map for the sample processed up to $\gamma = 68$.

phase lamellae is much lower than 50 nm. Further, the feeble and incomplete ring pattern in the corresponding SADP indicated towards partial nano-structuring (Fig. 8(b)). Interestingly, at $\gamma = 68$ certain regions underwent severe nano-structuring, as is evident from the well-defined ring pattern obtained from such regions. Fig. 9(a) presents a TEM BF micrograph exhibiting such HCP nano-crystallites in the

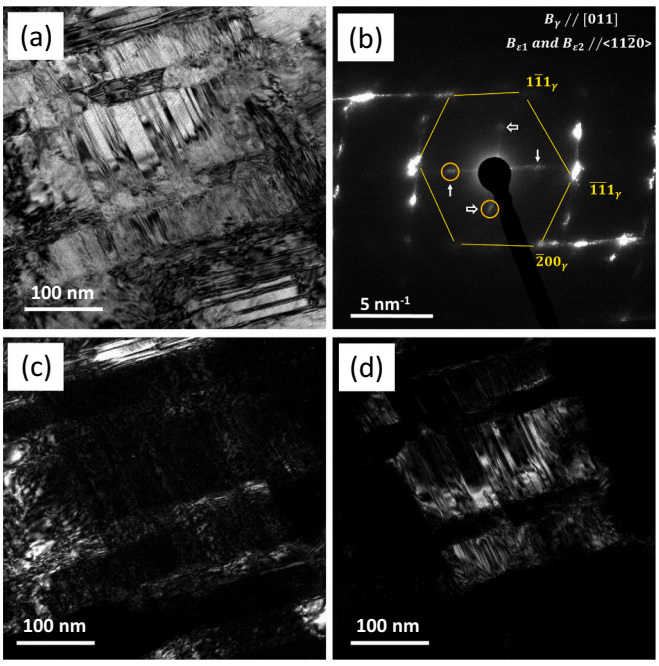

Fig. 6. (a) TEM BF micrograph of the specimen processed up to $\gamma = 15$; (b) corresponding SADP; (c) and (d) DF micrograph showing two variants of HCP phase corresponding to the $< 11\bar{2}0 >$ zone axis.

specimen which suffered shear strain of 68. The corresponding SADP showed the presence of ring pattern which is indexed with respect to the HCP phase (Fig. 9(b)). The TEM DF micrograph imaged using the encircled spot illuminated the nano-crystallites corresponding to the HCP phase (Fig. 9(c)). Such a fine HCP phase can contribute significantly to the strengthening of the material when deformed. Although HPT processing is well-known to promote nano-structuring [28], the only report published on the HPT processing of the studied alloy reported the retention of the original grain size after the processing [19]. It is worth noting that, in the above study, the HPT processing was carried out at a lower pressure of 4 GPa compared to 6 GPa in the present work [19]. Hence, it seems that there is a threshold pressure, only above which nano-structuring is possible in the present alloy.

3.2. Microstructural characterization by XLPA

TEM investigation indicated the activation of non-basal planes during HPT processing (Fig. 7). XLPA employing the CMWP fitting method confirmed and quantified the different types of active dislocations in various HCP planes. Fig. 10(a) presents the experimentally observed XRD pattern of the HEA after processed up to $\gamma = 68$, in which the corresponding pattern calculated from the CMWP fitting method was overlapped. The difference between the experimental and the calculated pattern was near to zero and hence the quality of the fitting was good. During the CMWP evaluation, the peaks of the HCP phase were fitted while the reflections of the FCC phase were put into the background. For FCC peaks appearing on the pattern, the spline was drawn in such a way that it incorporates both the real background and the FCC peak. The theoretical pattern used for fitting was the sum of this background and the calculated hcp peaks. An instance is shown in Fig. 10(b) for a complex case where there is an overlap between the {111} FCC and {0002} HCP peaks. A good quality of fitting was also obtained for the case of $\gamma = 15$ and has not been shown separately. Evolution of the microstructural parameters belonging to the HCP phase obtained from the CMWP analysis are listed in Table 1. Interestingly, the area weighted mean crystallite size ($<x>_{area}$) of the HCP phase was 16–17 nm for both HPT-processed HEA, i.e., the crystallite size already saturated even after $\gamma = 15$, possibly due to massive defect generation during the HPT processing. The tendency towards nano-structuring of the grains after $\gamma = 15$ and $\gamma = 68$ has already been confirmed in the TEM images (Figs. 8 and 9, respectively). Hence, apart from the $\gamma \rightarrow \varepsilon$ phase transformation, simultaneous nano-structuring of the newly formed HCP phase was a major plastic deformation event during HPT processing. Further, the dislocation density (ρ) had a very high value of 51×10^{14} m^{-2} even at $\gamma = 15$ which further increased to 71×10^{14} m^{-2} at $\gamma = 68$.

Activation of various dislocation types in the HCP phase can have important implications towards accomplishment of homogenous deformation. XLPA confirmed the activation of <c> and <c+a> dislocations during HPT processing. It is worth noting that <a> type dislocations constituted nearly 50% of the slip both after $\gamma = 15$ and $\gamma = 68$. Although the combined contribution of non-basal <c> and <c+a> dislocations remained consistent, their individual contributions varied dramatically (Table 1) with increase in the shear strain. Specimen deformed up to $\gamma = 15$ showed predominance of <c> type screw dislocation whereas <c+a> dislocations were nearly absent. An observation of <c> dislocation, mostly of screw type, in plenty was also confirmed from the Williamson-Hall (WH) plot, modelled using the calculated dislocation-induced strain broadening due to screw dislocations corresponding to

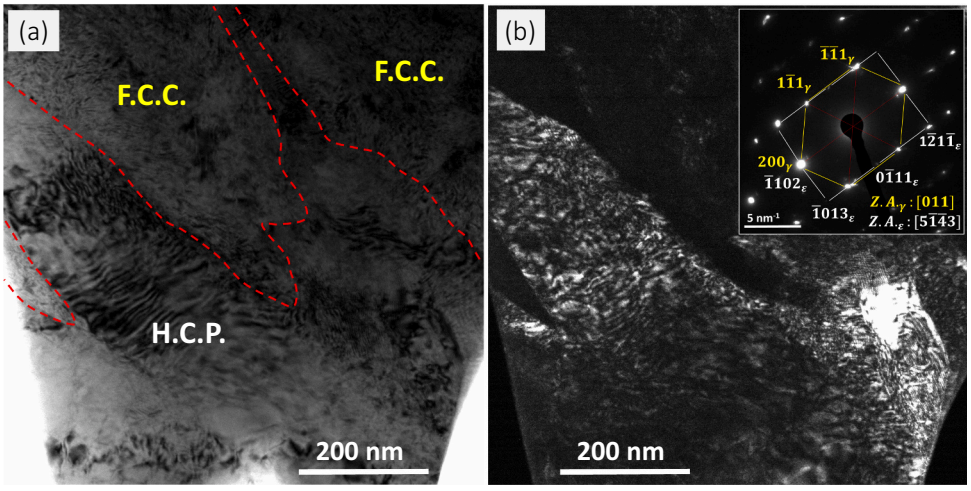

Fig. 7. (a) TEM BF micrograph of the specimen processed up to $\gamma = 68$ showing HCP and FCC phases distinctly; (b) corresponding DF micrograph (inset shows the indexed SADP).

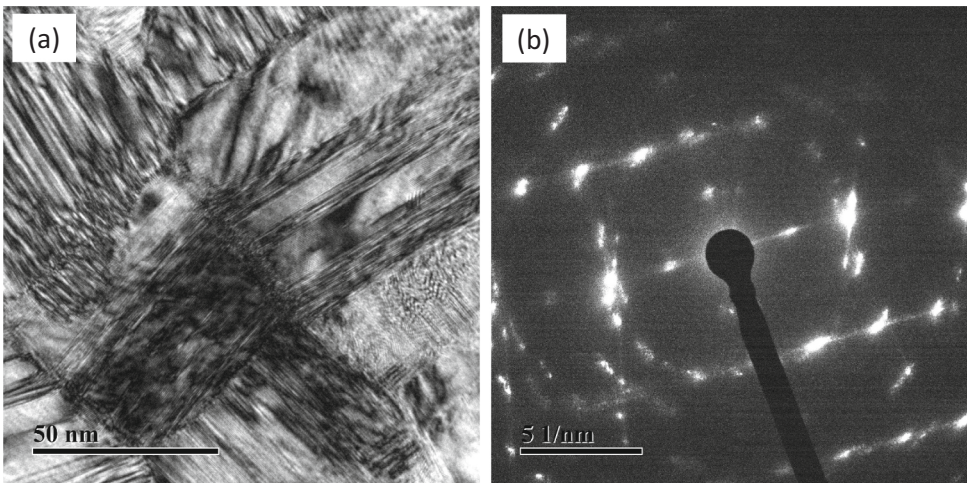

Fig. 8. (a) TEM BF micrograph of the specimen deformed up to $\gamma = 15$, showing the presence of HCP and FCC phases; (b) corresponding SADP showing the initiation of ring pattern formation.

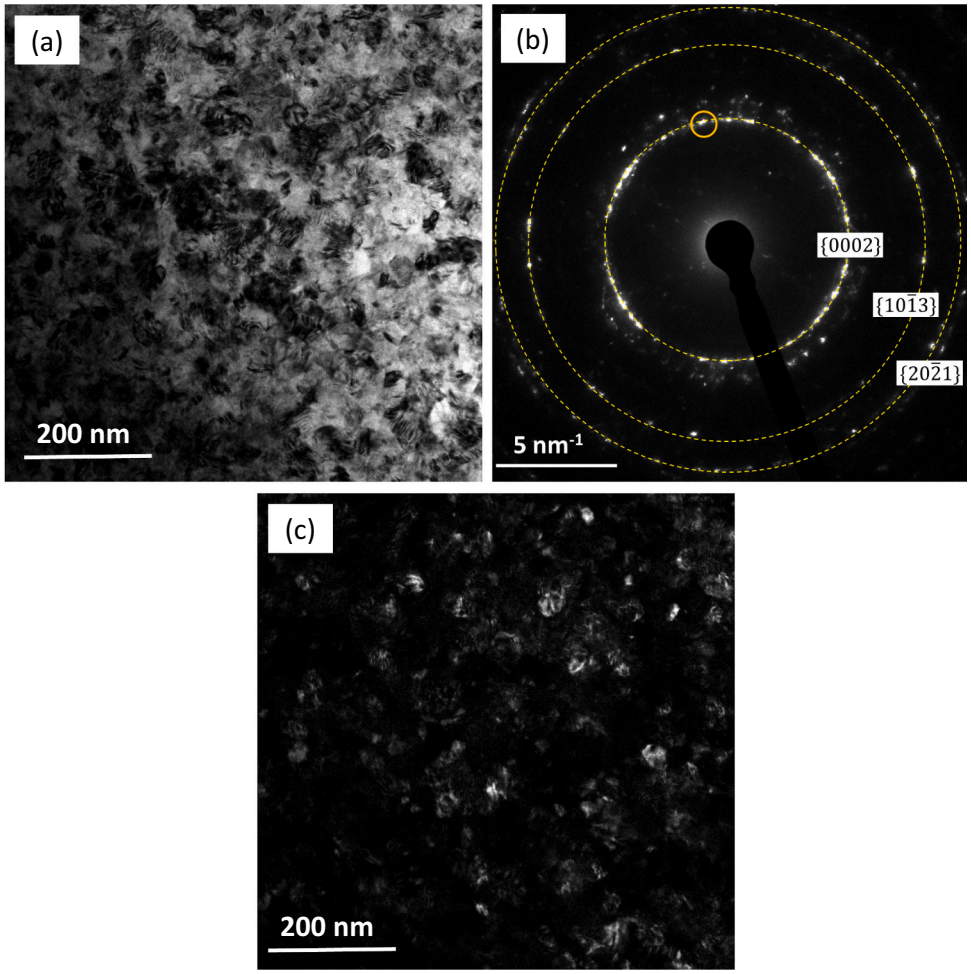

Fig. 9. (a) TEM BF micrograph of the specimen processed up to $\gamma = 68$; (b) SADP showing a ring pattern which indicates the occurrence of nano-structuring; (c) corresponding DF micrograph, imaged from the encircled spot, showing the formation of nano-crystallites corresponding to the HCP phase.

each of the diffraction peak for the specimen after $\gamma = 68$ (Fig. 10(c)). Trends of peak broadening in the modelled and the experimental WH plots showed good agreement, confirming the significant presence of <c> type screw dislocations. It is noted that the measured broadening is generally higher than the calculated widths in Fig. 10(c) since in the latter breadths only the dislocation broadening was considered without the contribution of the small crystallite size.

Fig. 11 presents the hardness values of the as-received and HPT-processed specimens. Hardness value increased by more than 2 times in the specimen processed up to $\gamma = 15$ as compared to the starting

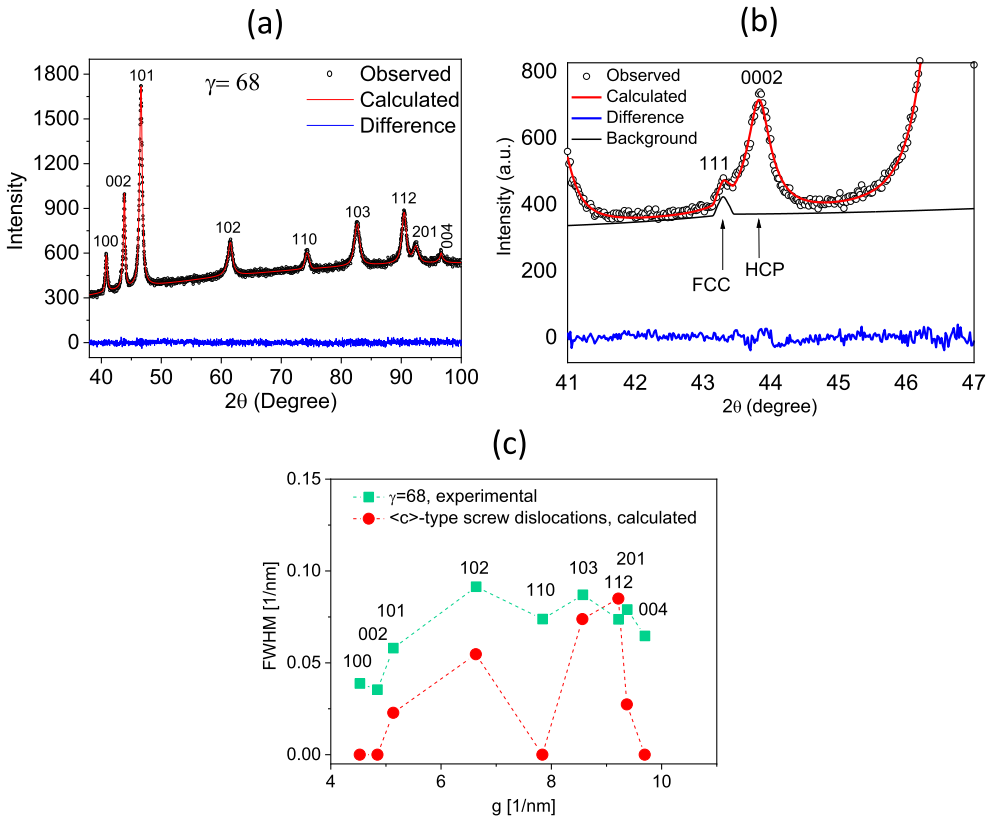

Fig. 10. (a) CMWP fitting of the experimentally observed XRD pattern for the specimen processed up to $\gamma = 68$; (b) an instance of background correction for a limited 2θ range in the specimen processed up to $\gamma = 68$; (c) a comparison between the experimentally observed and the theoretically calculated broadening due to <c>-type screw dislocations corresponding to each of the diffraction peak in the specimen processed up to $\gamma = 68$.

Table 1
Values of the microstructural parameters obtained from CMWP method.

Microstructural parameter	$\gamma = 15$	$\gamma = 68$
Area avg. crystallite size <x> area [nm]	17 ± 2	16 ± 2
Dislocation density ρ [10^{14} m^{-2}]	51 ± 6	71 ± 8
<a> type dislocations [%]	48 ± 6	47 ± 6
<c> type dislocations [%]: *Majority Screw*	51 ± 4	34 ± 4
<c+a> type dislocations [%]	1 ± 1	19 ± 5

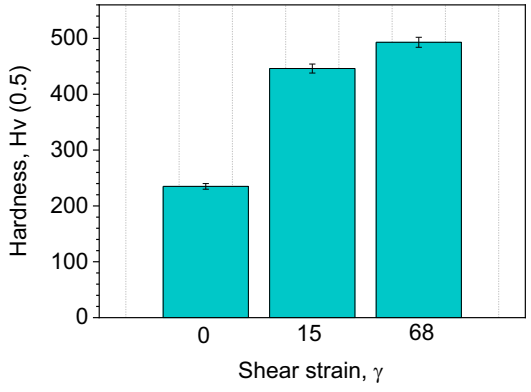

Fig. 11. Hardness evolution during HPT processing.

material. Hardness value further increased at $\gamma = 68$ in comparison to $\gamma = 15$. Successive improvement in the hardness value could be associated with the evolution of microstructure during the HPT processing, as shown in the above text.

4. Discussion

The present work investigates the evolution of microstructure in a HEA, $Fe_{40}Mn_{40}Co_{10}Cr_{10}$, during HPT processing for ½ and 2 turns. At the shear strain level (γ) of 15 and 68 for the ½ and 2 turns processing, respectively, a massive dislocation generation occurred which was in the order of 10^{15} m^{-2}. Significant extent of FCC➔HCP transformation was observed even at a processing up to $\gamma = 15$ and therefore the strain accommodation mechanism(s) in the transformed HCP phase is of interest from the viewpoint of hardening behaviour of this alloy. Hence, an emphasis has been laid on determination of dislocation mediated strain accommodation mechanism(s). To this end, an interesting observation of strain accommodation via significant occurrence of the non-basal slip in newly formed HCP phase was made, which is important with regards to the achievement of superior mechanical properties in this alloy. The following text discusses two important phenomena occurring during the HPT transformation of the studied alloy: (i) $\gamma \rightarrow \varepsilon$ phase transformation (ii) occurrence of non-basal slip in the HCP phase.

4.1. $\gamma \rightarrow \varepsilon$ phase transformation

The investigated HEA, $Fe_{40}Mn_{40}Co_{10}Cr_{10}$, is known to possess good strength – ductility combination during the tensile deformation [18] which is primarily attributed to work hardening delivered by extensive formation of deformation twins [18]. For this reason, this alloy has even been termed as “TWIP HEA” [18]. The present study, however, revealed an enormous occurrence of TRIP phenomena ($\gamma \rightarrow \varepsilon$ phase transformation) during the HPT processing. Hence, there should be an investigation to understand this starkly different deformation response of the same alloy under different processing conditions, viz., uniaxial tensile tests and high pressure torsion.

It is well known that formation of deformation induced HCP phase

requires an occurrence of intrinsic stacking faults in every second {111} plane of the γ phase [14]. As per the classical SFE-deformation behaviour correlation, FCC materials with SFE > 40–45 mJ/m^{-2} is known to deform primarily via slip process while with an intermediate SFE in the range of 20–45 mJ/m^{-2}, the deformation is mediated via twinning [29,30]. Furthermore, with SFE < 18–20 mJ/m^{-2}, TRIP is believed to be a major deformation mechanism [29,30]. For the present alloy, the SFE of the γ phase was theoretically predicted as 14–22 mJ/m^2 [7]. Although the actual range for $\gamma \rightarrow \varepsilon$ phase transformation has not been established yet for HEAs, the predicted SFE of the present HEA is in the lower side, which is expected to favour the martensitic transformation. However, a recent study experimentally determined the room temperature SFE of the presently studied alloy system to be 37.7 (±7) mJ/m^2 [31]. Considering the experimental SFE value, it seems that the alloy would not undergo TRIP effect in preference as dictated by the classical SFE-deformation behaviour correlation. One of the limiting factor for the $\gamma \rightarrow \varepsilon$ phase transformation is the increase in the critical stress required for the same with increase in SFE [32]. The high requirement of critical stress can be overcome at high applied stresses during deformation. In this context, the formation of ε phase in the present alloy has been reported at high strain level (corresponding to the stress level ~ 500 MPa) during tensile deformation at room temperature (RT) [33]. It is important to note that the volume fraction of the deformation-induced ε phase formed during uniaxial tension at RT was significantly low (~9%) and the same formed just before the fracture at true strain of ~0.35 [33]. There was no evidence of $\gamma \rightarrow \varepsilon$ phase transformation at early strain levels (or at low applied stress regime) during deformation at RT [33]. It is worth noting that the shear strain is considerably higher in the present case after ½ HPT turn, which resulted in transformation to HCP phase in ~75% of the volume of material. These observations suggested towards the kinetically constrained nature of $\gamma \rightarrow \varepsilon$ phase transformation in the present alloy. This is possibly due to requirement of high critical stress for the execution of $\gamma \rightarrow \varepsilon$ phase transformation event, which can be overcome by the application of high pressure. A further increase in the fraction of transformed HCP phase from ~75% to ~91% with an increase in the shear strain, γ from 15 to 68 alludes towards tendency of TRIP effect, provided the material is subjected to a suitably high pressure/strain.

4.2. Non-basal slip in transformed HCP phase

As a considerable fraction of HCP phase (75%) formed at relatively low shear strain ($\gamma = 15$), the subsequent strain accommodation ability would depend on the plastic deformation mechanism(s) of the transformed HCP phase. In this regard, characterization and quantification of dislocation types in the HCP phase is reported for the first time in this system.

Characterization of the slip behaviour of the HCP phase revealed a nearly equal occurrence of basal and non-basal dislocations (Table 1). Slip via non-basal type dislocations can improve the ductility in an otherwise brittle HCP phase. c/a ratio governs the activation of non-basal dislocations. In the present study, c/a ratio of the transformed HCP phase was determined to be ~1.62, which did not change during the HPT processing. Similar observation has been reported for an equiatomic FeMnCoCrNi alloy during high pressure compression [10]. c/a ratio is an intrinsic materials property and does not change as a function of external treatment such as deformation, heat treatment etc. Nevertheless, a few recent reports have indicated the possibility of c/a ratio alteration with imposition of very large strain [4,34]. In the present study, HPT processing up to 2 turns corresponds to a shear strain value of ~68. Despite such a large shear strain, a constant c/a ratio observed during the HPT processing is perhaps due to simultaneous strain accommodation via the active $\gamma \rightarrow \varepsilon$ phase transformation [4]. Importantly, c/a ratio lower than the ideal value of 1.633, which corresponds to the hard sphere model, favours prismatic <c> slip or pyramidal <c+a> slip [16]. The $Fe_{50}Mn_{30}Co_{10}Cr_{10}$ alloy with c/a ratio of 1.616 is reported earlier to form <c+a> and <c> dislocations during the tensile deformation [17]. Likewise, in the present case, c/a ratio of ~1.62 triggered the activation of both <c> and <c+a> dislocations along with the <a> type dislocations in the HPT processed specimens. Firstly, a high share of <a> dislocation is reasonable because of the significantly lower critical resolved shear stress (CRSS) for basal slip than prismatic and/or pyramidal slip [35]. Further, ~ 50% of the active dislocations were of <c> and <c+a> type, which essentially constitute non-basal slip. Such a high contribution of non-basal slip in overall strain accommodation mechanism of HCP phase is consistent with the measured c/a ratio being lower than the ideal value of 1.633. Interestingly, the propensity of <c> type dislocations was considerably higher than the <c+a> type dislocations in both the ½ and 2 turns processed specimens ($\gamma = 15$ and 68, respectively). Formation of <c> dislocations in preference is an unexpected observation as these are considered to be sessile [36]. Such an anomalous dislocation activity can be attributed to the inherent tendency of <c+a> dislocations, having larger Burgers vector, to dissociate into <c> and <a> types of dislocations, which minimizes the elastic strain energy [37]. TEM investigation showed evidence of dislocation activities in pyramidal plane, which indicates the formation of <c+a> dislocations (Fig. 7). The XLPA measurements indicated high populations of <c> dislocations in the HPT-processed specimens which confirms the energetically favourable dissociation of <c+a> into <c> and <a> types of dislocations. Further, the fraction of <c+a> dislocations, which were virtually non-existent at $\gamma = 15$ increased to ~19% at $\gamma = 68$ (Table 1). This is possibly to accommodate the successive strain imposed in the HEA, which might have not been possible by the already generated sessile <c> dislocations. However, the presence of <c> dislocations with a screw character in majority can be advantageous for accommodating plastic deformation at higher strain levels, owing to their tendency to cross-slip. Multiple cross-slip can assist in spreading the dislocation activity in various intersecting planes and thereby leading to homogenous deformation.

Formation of both the <c> and <c+a> dislocations (non-basal slip) in the HCP phase during severe plastic deformation is an important phenomenon with regards to the formability of the HEAs of similar compositions. Non-basal slip is required to complement the basal slip in order to achieve homogenous plasticity and thereby to accomplish the required formability. Hence, the formation of the transformed HCP phase with a c/a ratio correctly tuned to a value <1.633 can prove to be highly advantageous from the viewpoint of developing a strong and ductile HEA [17].

Finally, a significant improvement in the hardness with increase in the shear strain was observed with respect to the starting material (Fig. 11). Such enhancement in the hardness values by more than two times can be attributed to a combination of co-existing strengthening mechanisms namely, TRIP mechanism, dislocation strengthening and grain refinement [37]. In the context of strengthening via grain refinement, it is to be noted that a complete nano-structuring was not obtained after the 2 turns of HPT processing or equivalently after shear strain, $\gamma = 68$. HPT processing is known to yield inhomogeneous/gradient microstructure in an early stage of plastic deformation, i.e., generally below 5 turns [28]. Therefore, two turns of HPT processing was not sufficient enough to generate the homogeneous microstructure in most metals and HEAs [38,39] and due to this fact we observed various regions showing nano-structuring (Fig. 9) while others not (Figs. 5 and 7).

5. Conclusions

The present study investigates the evolution of microstructure during the high pressure torsion processing of a $Fe_{40}Mn_{40}Co_{10}Cr_{10}$ high entropy alloy. The following conclusions are drawn from this study:

1. HPT processing up to shear strain, $\gamma = 15$ produced significant TRIP effect in a HEA which otherwise demonstrates predominantly TWIP behaviour during quasi-static uniaxial tensile tests.

2. While the fraction of transformed HCP phase increased from ~75% to ~91% by increasing the shear strain, γ from 15 to 68, its c/a ratio remained nearly constant at 1.62. A c/a ratio < 1.633 manifested as the prominent occurrence of non-basal slip (at least 50%) at both $\gamma =$ 15 and 68. Despite no change in the c/a ratio of the transformed HCP phase with increasing strain, there was a prominent difference in the micro-mechanism of plastic deformation as reflected by a considerable change in the fractions of <c> and <c+a> type dislocations.
3. HPT processing was accompanied with a significant increase in the dislocation density of HCP phase. A 40% increase in dislocation density was noted while increasing the shear strain, γ from 15 to 68.
4. Unlike a continued increase in TRIP effect and dislocation density, there was a saturation in the crystallite size even for shear strain, $\gamma =$ 15. Prominent nano-structuring was achieved at $\gamma = 68$ as evidenced by TEM investigations.
5. Significant hardening was achieved by HPT processing as confirmed by the two fold increase in hardness for specimen deformed up to shear strain, $\gamma = 15$. This was attributed to a number of co-operative strengthening mechanisms, namely, Taylor hardening, grain refinement, martensitic/second phase strengthening.

Data availability statement

Data will be made available on request.

Declaration of Competing Interest

The authors declare that they have no known competing financial interests or personal relationships that could have appeared to influence the work reported in this paper.

Acknowledgements

This work was funded by CSIR-National Metallurgical Laboratory, India, under *i*-PSG mode; Project number: OLP 0346. A part of the work was completed in the ELTE Institutional Excellence Program (TKP2020-IKA-05) financed by Hungarian Ministry of Human Capacities. Further, the study was supported in part by the National Science Foundation of the United States under Grant No. DMR-1810343.

References

[1] B. Gludovatz, A. Hohenwarter, D. Catoor, E.H. Chang, E.P. George, R.O. Ritchie, A fracture-resistant high-entropy alloy for cryogenic applications, Science 345 (2014) 1153–1158, https://doi.org/10.1126/science.1254581.
[2] Z.F. He, N. Jia, D. Ma, H.L. Yan, Z.M. Li, D. Raabe, A Joint contribution of transformation and twinning to the high strength- ductility combination of a FeMnCoCr high entropy alloy at cryogenic temperatures, Mater. Sci. Eng. A 759 (2019) 437–447, https://doi.org/10.1016/j.msea.2019.05.057.
[3] Z. Li, K.G. Pradeep, Y. Deng, D. Raabe, C.C. Tasan, Metastable high-entropy dual-phase alloys overcome the strength-ductility trade-off, Nature. 534 (2016) 227–230, https://doi.org/10.1038/nature17981.
[4] S. Sinha, S.S. Nene, M. Frank, K. Liu, P. Agrawal, R.S. Mishra, On the evolving nature of c/a ratio in a hexagonal close-packed epsilon martensite phase in transformative high entropy alloys, Sci. Rep. (2019) 1–14, https://doi.org/10.1038/s41598-019-49904-5.
[5] S.S. Nene, M. Frank, K. Liu, R.S. Mishra, B.A. Mcwilliams, K.C. Cho, Extremely high strength and work hardening ability in a metastable high entropy alloy, Sci. Rep. (2018) 1–8, https://doi.org/10.1038/s41598-018-28383-0.
[6] S. Zhao, G.M. Stocks, Y. Zhang, Stacking fault energies of face-centered cubic concentrated solid solution alloys, Acta Mater. 134 (2017) 334–345, https://doi.org/10.1016/j.actamat.2017.05.001.
[7] S. Huang, H. Huang, W. Li, D. Kim, S. Lu, X. Li, E. Holmström, S.K. Kwon, L. Vitos, Twinning in metastable high-entropy alloys, Nat. Commun. 9 (2018) 1–7, https://doi.org/10.1038/s41467-018-04780-x.
[8] Y.H. Zhang, Y. Zhuang, A. Hu, J.J. Kai, C.T. Liu, The origin of negative stacking fault energies and nano-twin formation in face-centered cubic high entropy alloys, Scr. Mater. 130 (2017) 96–99, https://doi.org/10.1016/j.scriptamat.2016.11.014.
[9] H. Huang, X. Li, Z. Dong, W. Li, S. Huang, D. Meng, X. Lai, T. Liu, S. Zhu, L. Vitos, Critical stress for twinning nucleation in CrCoNi-based medium and high entropy alloys, Acta Mater. 149 (2018) 388–396, https://doi.org/10.1016/j.actamat.2018.02.037.
[10] F. Zhang, Y. Wu, H. Lou, Z. Zeng, V.B. Prakapenka, E. Greenberg, Y. Ren, J. Yan, J. S. Okasinski, X. Liu, Y. Liu, Q. Zeng, Z. Lu, Polymorphism in a high-entropy alloy, Nat. Commun. 8 (2017) 1–7, https://doi.org/10.1038/ncomms15687.
[11] C.L. Tracy, S. Park, D.R. Rittman, S.J. Zinkle, H. Bei, M. Lang, R.C. Ewing, W. L. Mao, High pressure synthesis of a hexagonal close-packed phase of the high-entropy alloy CrMnFeCoNi, Nat. Commun. 8 (2017) 1–6, https://doi.org/10.1038/ncomms15634.
[12] J. Gubicza, P.T. Hung, M. Kawasaki, J.-K. Han, Y. Zhao, Y. Xue, J.L. Labar, Influence of severe plastic deformation on the microstructure and hardness of a CoCrFeNi high entropy alloy: a comparison with CoCrFeNiMn, Mater. Charact. 154 (2019) 304–314, https://doi.org/10.1016/j.matchar.2019.06.015.
[13] A. Heczel, M. Kawasaki, J.L. Labar, J. Jang, T.G. Langdon, J. Gubicza, Defect structure and hardness in nanocrystalline CoCrFeMnNi high- entropy alloy processed by high-pressure torsion, J. Alloys Compd. 711 (2017) 143–154. https://doi.org/10.1016/j.jallcom.2017.03.352.
[14] H. Fujita, S. Ueda, Stacking faults and f.c.c. (γ) → h.c.p. (ϵ) transformation in 188-type stainless steel, Acta Metall. 20 (1972) 759–767, https://doi.org/10.1016/0001-6160(72)90104-6.
[15] M.H. Yoo, S.R. Agnew, J.R. Morris, K.M. Ho, Non-basal slip systems in HCP metals and alloys: source mechanisms, Mater. Sci. Eng. A 321 (2001) 87–92, https://doi.org/10.1016/S0921-5093(01)01027-9.
[16] F.E. Hauser, P.R. Landon, J.E. Dorn, Fracture of magnesium alloys at low temperature, Trans. Am. Inst. Min. Metall. Eng. 206 (1956) 589–593.
[17] Y. Bu, Z. Li, J. Liu, H. Wang, D. Raabe, W. Yang, Nonbasal slip systems enable a strong and ductile hexagonal-close-packed high-entropy phase, Phys. Rev. Lett. 122 (2019) 75502, https://doi.org/10.1103/PhysRevLett.122.075502.
[18] Y. Deng, C.C. Tasan, K.G. Pradeep, H. Springer, A. Kostka, D. Raabe, Design of a twinning-induced plasticity high entropy alloy, Acta Mater. 94 (2015) 124–133, https://doi.org/10.1016/j.actamat.2015.04.014.
[19] P. Sathiyamoorthi, P. Asghari-rad, G.M. Karthik, Z. Alireza, H.S. Kim, Unusual strain induced martensite and absence of conventional grain refinement in twinning induced plasticity high-entropy alloy processed by high-pressure torsion, Mater. Sci. Eng. A 803 (2020) 140570, https://doi.org/10.1016/j.msea.2020.140570.
[20] R.B. Figueiredo, P. Henrique, R. Pereira, M. Teresa, P. Aguilar, P.R. Cetlin, T. G. Langdon, Using finite element modeling to examine the temperature distribution in quasi-constrained high-pressure torsion, Acta Mater. 60 (2012) 3190–3198, https://doi.org/10.1016/j.actamat.2012.02.027.
[21] W. Skrotzki, A. Pukenas, B. Joni, E. Odor, T. Ungar, A. Hohenwarter, R. Pippan, E. P. George, Microstructure and texture evolution during severe plastic deformation of CrMnFeCoNi high-entropy alloy, IOP Conf. Ser. Mat. Sci. Engg. 194 (2017), 012028, https://doi.org/10.1088/1757-899X/194/1/012028.
[22] J. Gubicza, X-Ray Line Profile Analysis in Materials Science, IGI Global, Hershey, USA, 2014.
[23] G. Ribárik, J. Gubicza, T. Ungár, Correlation between strength and microstructure of ball milled Al-Mg alloys determined by X-ray diffraction, Mater. Sci. Eng. A 387-389 (2004) 343–347, https://doi.org/10.1016/j.msea.2004.01.089.
[24] K. Máthis, G. Csiszár, J. Capek, J. Gubicza, B. Clausen, P. Lukás, A. Vinogradov, S. R. Agnew, Effect of the loading mode on the evolution of the deformation mechanisms in randomly textured magnesium polycrystals: comparison of experimental and modeling results, Int. J. Plast. 72 (2015) 127–150, https://doi.org/10.1016/j.ijplas.2015.05.009.
[25] A. Borbély, I. Dragomir-Cernatescu, G. Ribárik, T. Ungár, Computer program ANIZC for the calculation of diffraction contrast factors of dislocations in elastically anisotropic cubic, hexagonal and trigonal crystals, J. Appl. Crystallogr. 36 (2003) 160–162, https://doi.org/10.1107/S0021889802021581.
[26] X. Li, D.L. Irving, L. Vitos, First-principles investigation of the micromechanical properties of fcc-hcp polymorphic high-entropy alloys, Sci. Rep. 8 (1) (2018) 1–8, https://doi.org/10.1038/s41598-018-29588-z.
[27] L. Lutterotti, S. Matthies, H.-R. Wenk, MAUD (material analysis using diffraction): a user friendly Java program for Rietveld texture analysis and more, Proc. Twelfth Int. Conf. Textures Mater. 1 (1999) 1599–1604.
[28] A.P. Zhilyaev, T.G. Langdon, Using high-pressure torsion for metal processing: fundamentals and applications, Prog. Mater. Sci. 53 (2008) 893–979, https://doi.org/10.1016/j.pmatsci.2008.03.002.
[29] S. Curtze, V. Kuokkala, Dependence of tensile deformation behavior of TWIP steels on stacking fault energy, temperature and strain rate, Acta Mater. 58 (2010) 5129–5141, https://doi.org/10.1016/j.actamat.2010.05.049.
[30] S. Allain, J.P. Chateau, O. Bouaziz, S. Migot, N. Guelton, Correlations between the calculated stacking fault energy and the plasticity mechanisms in Fe-Mn-C alloys, Mater. Sci. Eng. A 387–389 (2004) 158–162, https://doi.org/10.1016/j.msea.2004.01.059.
[31] A.K. Chandan, S. Tripathy, B. Sen, M. Ghosh, S. Ghosh Chowdhury, Temperature dependent deformation behavior and stacking fault energy of Fe40Mn40Co10Cr10 alloy, Scr. Mater. 199 (2021) 113891, https://doi.org/10.1016/j.scriptamat.2021.113891.
[32] S.L. Wong, M. Madivala, U. Prahl, F. Roters, D. Raabe, A crystal plasticity model for twinning- and transformation-induced plasticity, Acta Mater. 118 (2016) 140–151, https://doi.org/10.1016/j.actamat.2016.07.032.
[33] A.K. Chandan, S. Tripathy, M. Ghosh, S.G. Chowdhury, Evolution of substructure of a non-equiatomic FeMnCrCo high entropy alloy deformed at ambient temperature, Metall. Mater. Trans. A. 50 (2019) 5079–5090, https://doi.org/10.1007/s11661-019- 05438-z.
[34] S. Djaziri, Y. Li, Gh.A. Nematollahi, B. Grabowski, S. Goto, C. Kirchlechner, A. Kostka, S. Doyle, J. Neugebauer, D. Raabe, G. Dehm, Deformation-induced

martensite: a new paradigm for exceptional steels, Adv. Mater. 28 (2016) 7753–7757, https://doi.org/10.1002/adma.201601526.
[35] Y.N. Wang, J.C. Huang, Texture analysis in hexagonal materials, Mater. Chem. Phys. 81 (2003) 11–26, https://doi.org/10.1016/S0254-0584(03)00168-8.
[36] Z. Wu, W.A. Curtin, Intrinsic structural transitions of the pyramidal I ⟨ c + a ⟩ dislocation in magnesium, Scr. Mater. 116 (2016) 104–107, https://doi.org/10.1016/j.scriptamat.2016.01.041.
[37] G.E. Dieter, Mechanical Metallurgy, McGraw Hill Book Company, UK, 1988.
[38] M. Kawasaki, Different models of hardness evolution in ultrafine-grained materials processed by high-pressure torsion, J. Mater. Sci. 49 (2014) 18–34, https://doi.org/10.1007/s10853-013-7687-9.
[39] Dong-Hyun Lee, In-Choi Choi, Moon-Young Seok, J. He, Z. Lu, Jin-Yoo Suh, M. Kawasaki, T.G. Langdon, Jae-il Jang, Nanomechanical behavior and structural stability of a nanocrystalline CoCrFeNiMn high-entropy alloy processed by high-pressure torsion, J. Mater. Res. 30 (2015) 2804–2815, https://doi.org/10.1557/jmr.2015.239.